

High-Pressure High-Temperature tailoring of High Entropy Alloys for extreme environments

Kirill V. Yusenko,^{1,2*} Sephira Riva,¹ Wilson A. Crichton,³ Kristina Spektor,³ Elena Bykova,⁴ Anna Pakhomova,⁴ Adam Tudball,⁵ Ilya Kupenko,⁶ Arno Rohrbach,⁶ Stephan Klemme,⁶ Francesco Mazzali,¹ Serena Margadonna,¹ Nicholas P. Lavery,¹ Stephen G.R. Brown¹

¹College of Engineering, Swansea University, Bay Campus, Swansea SA1 8EN, Wales, UK

²Institute of Solid State Chemistry, Pervomaiskaia str. 91, 620990 Ekaterinburg, Russia

³ESRF – The European Synchrotron, 71 Avenue des Martyrs, 38000, Grenoble, France

⁴Photon Sciences, Deutsches Elektronen-Synchrotron, Notkestrasse 85, D-22607 Hamburg, Germany

⁵Kennametal Manufacturing (UK) Ltd., Lake Road, Leeway Industrial Estate, Newport NP19 4SR, Wales, UK

⁶Institut für Mineralogie, Westfälische-Wilhelms-Universität Münster, Corrensstrasse 24, 48149 Münster, Germany

*E-mail address: k.yusenko@swansea.ac.uk

Abstract

The exceptional performance of some High Entropy Alloys (HEAs) under extreme conditions holds out the possibility of new and exciting materials for engineers to exploit in future applications. In this work, instead of focusing solely on the effects of high temperature on HEAs, the effects of combined high temperature and high pressure were observed. Phase transformations occurring in a pristine HEA, the as-cast *bcc*-Al₂CoCrFeNi, are heavily influenced by temperature, pressure, and by scandium additions. As-cast *bcc*-Al₂CoCrFeNi and *fcc*-Al_{0.3}CoCrFeNi HEAs are structurally stable below 60 GPa and do not undergo phase transitions. Addition of scandium to *bcc*-Al₂CoCrFeNi results in the precipitation of hexagonal AlScM intermetallic (*W*-phase), which dissolves in the matrix after high-pressure high-temperature treatment. Addition of scandium and high-pressure sintering improve hardness and thermal stability of well-investigated *fcc*- and *bcc*-HEAs. The dissolution of the intermetallic in the main phase at high pressure suggests a new strategy in the design and optimization of HEAs.

Keywords: High-Entropy Alloys; Scandium; High-pressure high-temperature sintering; Spark plasma sintering; *In situ* X-ray diffraction

1. Introduction

High Entropy Alloys (HEAs) present a formidable array of compositional complexity and rich microstructural variation. Exploration of this enormous variable space only began in 2004 [1,2]. The unexplored central regions of the hyper-dimensional composition space of multicomponent alloys, away from the edges, faces and vertices, can reveal new alloys of scientific and practical significance. In early works, HEAs have been reported to crystallize as single-phase solid solutions, where atoms are randomly distributed [3]. The later discovery of sub-ordered solutions and intermetallic compounds displaying long-range order challenge the traditional definitions of HEAs and open the road for the rationalization and control of mechanical and functional properties [4-6]. Attractive features, especially under extreme impact, have already been reported for single-phase HEAs systems [7,8]. Nevertheless, as in many of the most advanced structural alloys, the properties of HEAs can be further tuned by proper control of the size, shape, volume fraction and distribution of intermetallic phases [9]. Precipitation hardening represents an effective strengthening mechanism, as reported for the Al—Co—Cr—Cu—Fe—Ni [10,11] and Al—Cr—Fe—Mn—Ni [12] multicomponent systems. Further introduction of ordered nano-precipitates as pinning centres [13] can be achieved by selective annealing [14,15] or by the addition of alloying elements [16]. These intermetallics require stabilization to maintain coherence without disrupting the matrix [17,18].

Scandium represents a promising candidate to achieve coherent, homogeneously dispersed ordered phases in HEAs, due to the large number of binary and ternary compounds with low formation enthalpy and high thermal stability that scandium forms with most elements in the periodic table.

As soon as mechanical properties depend on microstructure and composition. Microstructural features such as distribution, shape and size of the phases or the presence of defects influences mechanical properties just as profoundly [9]. Both parameters are strictly connected to synthetic conditions and post-synthetic mechanical and/or heat treatments [19]. Since HEAs have been proposed for applications in extreme environments, their phase evolution upon heating has been extensively studied, both *in situ* and *ex situ* [5]. So, the exploration of the hyper-dimensional

stability space of HEAs systems at different pressure and temperature conditions has barely been tackled. Even for sintering (a common processing route for manufacturing bulk polycrystalline materials), the effect of pressure – rather than temperature – has rarely been studied [17-19].

A Spark Plasma Sintering (SPS) operates under relatively low pressure (below 0.1 GPa) nevertheless provides fast densification of powder-based precursor materials due to highly localized temperature increases caused by the application of pulsed current [20]. The pulsed current has a cleansing effect on particle surfaces, which results in very low or zero oxygen concentration at grain boundaries. Several HEAs have been consolidated [21,22] or synthesized [23] by SPS, the results give only a partial overview of the phase stability or the equation of state of the respective systems.

High-pressure investigation of *fcc*-structured CoCrFeNiMn [24] highlight the extraordinary potentials hidden in the pressure-dependent phase diagrams of multicomponent alloys. The role of pressure in the phase stability of phase pure and intermetallic containing HEAs is thus the second major component of the work presented here. A consistent high-pressure high-temperature (HP–HT) *in situ* investigation of microstructure evolution and phase transformation in *B2*-structured Al₂CoCrFeNi and Sc-containing Al₂CoCrFeNi is reported in the current study.

2. Experimental details

2.1. Materials and primary characterization

fcc-Al_{0.3}CoCrFeNi, *bcc*-Al₂CoCrFeNi and *bcc*-Al₂CoCrFeNi + 3 at.% Sc were prepared using induction melting from powders of pure metals. Samples were melted in *h*-BN crucibles in an Ar filled glove-box. Complete melting of the samples was achieved above 1580 K. After 1-2 minutes at the melting temperature, the sample was cooled down naturally to room temperature. The samples were re-melted three times to ensure homogeneity. They were then powdered using a Fritsch Planetary Mill PULVERISETTE 5/2 (36 h, 250 r.p.m.) for *bcc*-Al₂CoCrFeNi and a Fritsch Mini-Mill Pulverisette 23 (10 min. at 50 r.p.m.) for *bcc*-Al₂CoCrFeNi + 3 at.% Sc. These samples are referred as *as-cast* in the text. For high-temperature annealing at ambient pressure, pellets of

each sample were sealed in a quartz tube under vacuum and heated in a furnace with the following specifications: *bcc*-Al₂CoCrFeNi at 1123, 12 h; *bcc*-Al₂CoCrFeNi + 3 at.% Sc at 1173 K, 12 h. After annealing, the tubes were quenched in ice water. Samples atomic compositions are summarized in Tables S1–S2.

For microstructure and elemental analysis, all samples were mounted in carbonised resin, polished using MetaDiTM Supreme Polycrystalline Diamond Suspension (1 μ m). As-cast and annealed samples at ambient pressure were etched with a 5 % solution of HNO₃ in ethanol. Morphology and elemental compositions were analysed using a Hitachi S-4800 Field Emission scanning-electron microscope (SEM) equipped with energy dispersive X-ray (EDX) analyser. The average elemental composition was obtained from 2.5×1.5 mm maps. Vickers hardness was measured on a WilsonR VH3100 Automatic Knoop/Vickers Hardness tester. 25 individual points under 9.81 N (1 kg) testing load were measured to obtain statistically significant results. Density was measured using flotation in water in the ATTENSION equipment. 5 measurements were averaged.

2.2. High-temperature in situ experiments

In situ high-temperature X-ray diffraction data for the powdered *bcc*-Al₂CoCrFeNi and *bcc*-Al₂CoCrFeNi + 3 at.% Sc samples were collected at the I-11 beam-line at the DIAMOND light source ($\lambda = 0.494984$ Å). A wide-angle position sensitive detector based on Mythen-2 Si strip modules was applied to collect the XRD data. The detector was moved at constant angular speed with 10 s scan time at each temperature and 60 s waiting time in order to let the temperature stabilize. The powdered alloys were sealed in 0.5 mm quartz capillaries in vacuum, and heated in the capillary furnace from 300 to 1400 K with axial rotation [25]. Oxidation has been detected above 1270 K, which is probably due to the reaction of the metallic alloy with quartz at high temperature, resulting in capillary destruction. Radial diffraction data were calibrated, corrected and integrated using v17 of the FIT2D software [26]. The same software was applied for plotting temperature and pressure dependent PXRD images. Cell parameters for selected PXRD patterns

were refined using TOPAS software [27]. LaB₆ (NIST SRM 660c) powder was used as the external standard for calibration for all diffraction experiments.

2.3. High-pressure high-temperature treatment

Bcc-Al₂CoCrFeNi and *bcc*-Al₂CoCrFeNi + 3 at.% Sc alloys were powdered using a ball-mill and further sintered under compression using piston-cylinder press at 2.1 GPa, and with two laboratory multi-anvil devices (sintering under 9.5 and 18.5 GPa compression) and in DACs (up to 60 GPa at RT). Piston-cylinder and multi-anvil presses allowed a recovery of specimens with the dimensions suitable for further mechanical characterization.

Heating of *bcc*-Al₂CoCrFeNi and *bcc*-Al₂CoCrFeNi + 3 at.% Sc at ambient pressure from 298 to 1270 K investigated *in situ* suggests a presence of several phase transitions above 870 K. For comparison, *bcc*-Al₂CoCrFeNi and *bcc*-Al₂CoCrFeNi + 3 at.% Sc were annealed at ambient pressure and spark-plasma sintered *bcc*-Al₂CoCrFeNi at 0.05 GPa above the respective transition temperatures. At the pressure of 2.1 GPa, *bcc*-Al₂CoCrFeNi and *bcc*-Al₂CoCrFeNi + 3 at.% Sc were annealed just below their corresponding melting temperature. Finally, the effect of temperature at 9.5 GPa was studied *in situ* up to 1500 K. All preparation conditions and corresponding phase compositions are reported in Table 1.

For SPS experiment, 300 g of *bcc*-Al₂CoCrFeNi powder were sintered using a FCT Systeme GmbH Spark Plasma Sintering Furnace type H-HP D 250 located at Kennametal Manufacturing (UK) Ltd. The tooling consisted of graphite punch and ring elements and carbon-fibre resistance heating elements. 0.35 mm graphite foil was used for lining the graphite elements. The powder under investigation was loaded into the mould. Only the graphite foil was in contact with the powder. To enable a DC current to pass through the tooling, water cooled rams are used, which clamp the tooling and apply force during sintering and conduct current through the tool and powder. The load provided to the tool from the rams was increased during the processing cycle:

- a) Achieve vacuum (less than 1mbar abs); contact load on rams of 10MPa;
- b) Heat tooling/powder at a uniform rate until 500°C is reached;

- c) Increase temperature at a ramp rate of 50°/min until 1123 K is reached; concurrent with this, the pressure on the powder is increased up to 50MPa (approx. 7.8MPa / min);
- d) The tool set is held at 1123 K for 10 minutes;
- e) Cooling phase for 1 min. during which time the load is removed; further cooling for 30 mins;
- f) Throughout the heating phases, a repeating pulsed DC current scheme was used of ‘36 ms pulse on’ and ‘8 ms pulse off’, as successfully reported for the consolidation of aluminium-based metal matrix composites [28].

Throughout the cooling phases, the vacuum was maintained until a temperature of less than 100°C was indicated when the vacuum was removed and the tooling retrieved.

The high-pressure experiments at 2.1 GPa were performed in an end-loaded piston cylinder apparatus installed at the Institut für Mineralogie, WWU Münster [29]. *bcc*-Al₂CoCrFeNi and *bcc*-Al₂CoCrFeNi + 3 at.% Sc powders were enclosed in a 2 mm alumina crucible. An alumina disk separated the samples. The pressure assembly consisted of a 1/2 inch talc-Pyrex assembly, which contained 6 mm diameter graphite heater in inner parts of crushable alumina. Temperature was monitored and controlled with a W₉₇Re₃-W₇₅Re₂₅ thermocouple. The assembly was pressed and heated simultaneously to 2.1 GPa and 1173 K, annealed for 60 minutes and finally quenched to room temperature.

Experiments at 9.5 GPa were performed on the large-volume press installed at the beam-line ID06-LVP, ESRF. X-ray diffraction data were collected using a linear pixelated GOS detector from Detection Technology at monochromatic wavelengths of 0.22542 Å. Powdered *bcc*-Al₂CoCrFeNi and *bcc*-Al₂CoCrFeNi + 3 at.% Sc alloy samples were loaded into a *h*-BN capsules, before being introduced into the windowed 10/4 MgO:Cr octahedral high-pressure assembly, along with a graphite furnace and ZrO₂ plugs. Pressure was generated using the 2000 tons MAVO Large-volume press in 6/8(x32) mode with tungsten 25 mm carbide anvils [30]. Pressures were estimated using the equation of state of *h*-BN and temperatures were estimated using the equation of state of MgO [31-34]. Samples have been compressed up to 9.5 GPa and heated up to 1000 K (without *in situ*

powder X-ray diffraction, PXRD, monitoring) or 1500 K (with *in situ* PXRD monitoring) under a constant pressure (Table 1). Heating was performed using a Delta Elektronika SM6000 power supply, by regulating constant voltage. Compressibility, heating, cooling and decompression curves were collected. The time resolution for PXRD patterns collected continuously on heating is 0.1 seconds, which are re-binned and written at 3.2 s interval and at 32 s interval on compression and decompression.

The 18 GPa experiments with *bcc*-Al₂CoCrFeNi and *bcc*-Al₂CoCrFeNi + 3 at.% Sc were performed in a 600 t multi-anvil device at the Institut für Mineralogie, WWU Münster. 10/4 assemblies were used with chromium-doped MgO octahedral, stepped LaCrO₃ furnaces and phyrophyllite gaskets. The assemblies were calibrated using the phase transition of Bi metal (room temperature) as well as the CaGeO₃ garnet-perovskite and coesite-stishovite phase transition (1100°C). The starting powders were encapsulated into polycrystalline crushable Al₂O₃ containers. The experiments were brought up to 18 GPa and further heated up to 1200°C at a rate of 10°C/min and then kept constant during 30 minutes. Samples were quenched by turning off the power supply, resulting in reducing the temperature to below 700 K in less than 1 s and decompressed overnight.

High-pressure PXRD data up to 61 GPa for *fcc*-Al_{0.3}CoCrFeNi and *bcc*-Al₂CoCrFeNi were collected at room temperature at the P.02.2. beam-line, PETRA III, DESY in Hamburg, ($\lambda = 0.29036 \text{ \AA}$, Perkin Elmer XRD1621 (2048x2048 pixels, 200x200 μm^2) flat panel detector, beam size 3(*v*)x3(*h*) μm^2). A membrane Mao-type diamond anvil cells with conically supported Boehler Almax type anvils (150 μm culet sizes) were used for pressure generation. Pressure was determined using a ruby luminescence below 40 GPa and Ne diffraction above 40 GPa. Neon was used as pressure-transmitting medium. The diffraction images were recorded under continuous ω -rotation of the DAC from -3 to +3° with 6 second acquisition time. After compression at room temperature, samples were laser-heated online up to 2000-2500°C from one side with simultaneous diffraction collection. For, *bcc*-Al₂CoCrFeNi melting did not occur below 2500°C at 60 GPa; *fcc*-Al_{0.3}CoCrFeNi was melted above 2650 °C at 60 GPa.

3. Results and discussion

Room temperature compressibility curves for *fcc*-Al_{0.3}CoCrFeNi and *bcc*-Al₂CoCrFeNi were fitted using the third-order Birch–Murnaghan isothermal equation of state (B-M EoS) [35], which fits experimental data better in comparison with other EoS (Figure 1). The volumetric thermal expansion coefficient for *bcc*-Al₂CoCrFeNi, $\alpha(T) = \alpha_0 + \alpha_1 T$, was obtained by fitting thermal dependence of its atomic volume: $\frac{V(T)}{Z} = \frac{V(T_0)}{Z} \exp \left[\int_{T_0}^T \alpha(T) dT \right]$ (Figure 1 inset, Table 2), where V/Z is atomic volume with a number of atoms in elemental cell $Z = 2$ for *bcc* and 4 for *fcc* structure. *fcc*-Al_{0.3}CoCrFeNi and *bcc*-Al₂CoCrFeNi do not show any phase change under room temperature compression below 60 GPa (Figure 1).

In as-cast *bcc*-Al₂CoCrFeNi sample, the presence of (1 0 0) super-lattice peak in the PXRD profile of the alloy (Figures 2 and 3) indicates long-range ordering (*B2* type) reported for Al-rich HEAs sub-lattice [36–39]. The lattice parameter of the as-cast alloy ($a = 2.877(2)$ Å) is consistent with the values reported by Kao [19]. The *bcc*-Al₂CoCrFeNi microstructure is dominated by large (~100 µm) grains and, unlike previous studies, does not show non-equiaxed dendrites [40,41] (Figure 4a). Chromium segregation is clearly visible in the as-cast material, but is reduced by heat treatment. The ordering of a metal in a high- or medium-entropy alloy has been previously reported to be spin-driven [42], with chromium ordering to be considered a way to eliminate magnetic frustration and lead to the reduction of free energy [43]. At ambient pressure, DSC results for *bcc*-Al₂CoCrFeNi display a sigmoid-like reversible transition at 890 K (Figure S1), associated by Gao in a theoretical work with the transition $bcc_1 + bcc_2 + B2 \rightarrow bcc + B2$ [44]. The divergence between the results reported here and Gao’s interpretation might arise from the profound differences in the crystal structure of the nominally equivalent starting material [36–39]. The decomposition of 40 wt.% of the *B2* phase above 890 K and the exsolution of a *fcc* phase ($a_{fcc1} = 3.636(8)$ Å) has been observed above 890 K. A second *fcc*₂ phase of lattice parameter $a_{fcc2} = 3.630(6)$ Å develops from the first *fcc* phase at 1023 K (65 wt.% *bcc*, 25 wt.% *fcc*₁, 10 wt.% *fcc*₂). From 1023 to 1273 K, *fcc*₂ grows

almost linearly (Figure S2). The *bcc*-Al₂CoCrFeNi sample annealed or sintered above the transition temperature should therefore display all three phases. However, neither the annealed nor the spark-plasma sintered sample's PXRD profiles reflect any change from the as-cast alloy (Figures 2a and 2c). Where the annealed pellet is concerned, the microstructure is dominated by nano-scale spherical particles, with features similar to those reported by Kao for annealing at 1173 and 1373 K (Figure 4c) [19,44,45].

Analogously, spark-plasma sintering of *bcc*-Al₂CoCrFeNi powder of 5–20 µm particle size results in homogeneous element distributions (Figure 4e). Despite intergranular porosity, grain growth has occurred with respect to the original particle size. Nevertheless, cracks and cavitations cause the macroscopic density of the spark-plasma sintered sample to be only 92.5 % of the density of the thermally annealed sample prepared at the same temperature ($d_{f, ann} = 6.4(1) \text{ g/cm}^3$ and $d_{f, SPS} = 5.92(7) \text{ g/cm}^3$ as established from flotation; $d_{XRD, ann} = 6.33(1) \text{ g/cm}^3$ and $d_{XRD, SPS} = 6.24(1) \text{ g/cm}^3$ as estimated from PXRD).

The main advantage of SPS is to achieve very high heating rates on materials where a fine grain size is desirable. SPS is comparable to Hot Pressing but the mechanism for heating differs with SPS providing a direct current through the powder. Hot Pressing is typically heated via radiation to the external surface of a container and hence the heating rate is relatively slow. It has been suggested that SPS direct current application enhances densification by promoting diffusion mechanisms over grain growth. Further, the process is characterised by the short process timescales which are preferred over slow and energy intensive processes.

It has been suggested that the direct current and, more specifically, the pulsed current has a cleaning effect on particle surfaces which in turn results in very low or absence of oxygen at grain boundaries. There is no evidence thus far on whether “plasma” is evident during SPS processing; however, the “cleaning” suggestion lends itself well to this idea [46].

Previous works on Ti based alloys have indicated that higher sintering temperatures and pressures have the most significant influence on the final density [47]. The feedstock particle size and

morphology have little if any influence on resulting material. The rate at which sintering occurs is mainly dependent on the heating rate although this is independent of the duration spent at the dwell temperature. Final grain size is also influenced by this factor. Other work has considered scaling up of this method and it has been found that the microstructure is maintained as uniform across a larger sample (up to 250 mm diameter) which is favourable when compared to hot pressing or other similar techniques. It is also interesting to note that alloys processed via this method would typically be subject to further thermomechanical processing in order to achieve not only a required near-net finished shape but also to achieve the required mechanical properties.

Low densification is still relevant with the high-pressure high-temperature treatment of *bcc*- $\text{Al}_2\text{CoCrFeNi}$ at 2.1 GPa and 1253 K. It results in inhomogeneity in the element distributions of Fe, Ni and Cr and the appearance of a fine lamellar microstructure along grain boundaries, similar to what was previously reported for spinodal decomposition in analogous systems [48-51]. Complete densification is achieved only with the sample treated at 9.5 GPa (Figure 4i). During the *in situ* PXRD experiments of room-temperature compression *B2* diffraction lines broaden due to induced inter-grain stress and strain as a result of multiphase nature of the sample.

The rapid exsolution of a secondary *fcc*-structured phase with $a = 3.623(7)$ Å from the original *B2* phase occurs above 740 K and can be followed from its (1 1 1), (2 0 0) and (1 1 0) diffraction lines. A second event occurs above 800 K, corresponding to the formation of a second unknown phase (possibly a primitive cubic phase). The *fcc* (1 1 1) diffraction line partly overlaps with the (2 0 0) MgO diffraction line (assembly material on the outer surface of the sample), but the (2 0 0) *fcc* line can be clearly followed. At 1500 K, the sample consists of *B2* phase and 6 wt.% *fcc* phase. Upon quenching, at 450 K the first *fcc* phase undergoes exsolution of a second *fcc*₂ phase, whereas the *B2* HP-HT phase can be quenched, recovered and further characterized. Its microstructure is similar to the original as-cast alloy, but does not exhibit nano-structuring (Figure 4e).

Vicker's hardness tests performed on the different *bcc*- $\text{Al}_2\text{CoCrFeNi}$ samples establish a direct dependence of hardness on the applied pressure (Figure 5). The as-cast material loses part of its

internal stress during annealing, causing a decrease in hardness. The spark-plasma sintered powder, having low densification between individual particles, displays less than half the original hardness. Surprisingly, however, HT treatments at 2.1 GPa and 9.5 GPa show an increase in hardness of almost 20 % compared to the original as-cast alloy.

In the light of the above results we have established the importance of pressure for the tuning of mechanical properties in HEAs. The combined influence of HP–HT treatments extends from *B2* phase stabilization to HT resistance, microstructure refinement and hardness enhancement.

Springing from its extraordinary influence on microstructure and mechanical properties of Al-based alloys, the term “scandium effect” came to define the benefits brought about by the precipitation of Sc-containing intermetallics in multicomponent alloys [52,53]. The addition of small (≤ 3 at.%) quantities of scandium to *bcc*–Al₂CoCrFeNi add a degree of complexity to the system and its phase diagram, but also affects the alloy’s mechanical properties. A 3 at.% Sc addition of scandium is enough to increase the hardness of the as-cast *bcc*–Al₂CoCrFeNi by almost 10 % (Figure 5).

At room temperature and ambient pressure, the as-cast *bcc*–Al₂CoCrFeNi + 3 at.% Sc alloy consists of a mixture of *B2*–structured matrix ($a = 2.88(2)$ Å) and a ternary hexagonal intermetallic (detected as three diffraction lines between 5.9–6.3°). Secondary phase can be associated with *W*–phase analogue AlCuSc (MgZn₂ type) in which Al and Cu sites are occupied by Al, Co, Fe or Ni [54]. The *W*–phase precipitates along grain boundaries causing grain refinement, whereas the *B2* matrix contains only a barely detectable amount of Sc (≤ 0.4 at.%) (Figures 4b and 4d).

The Sc-containing *bcc*–Al₂CoCrFeNi alloy undergoes a reversible transition between 1023 and 1073 K and displays a set of endothermic peaks at 1179 and 1239 K. The latter correspond to phase transition and melting/crystallisation of the *W*-phase. From *in situ* HT–PXRD we link the first DSC peak to the same *B2* to *fcc*₁+*fcc*₂ exsolution ($a_{\text{fcc1}} = 3.635(8)$ and $a_{\text{fcc2}} = 3.631(9)$ Å) occurring in the pristine *bcc*–Al₂CoCrFeNi alloy (Figure S2). The decomposition of the *B2* phase at ambient pressure occurs at a significantly higher temperature in the Sc-containing HEA (Figure 2b).

The main microstructural features of *bcc*-Al₂CoCrFeNi + 3 at.% Sc are maintained upon sintering at 2.1 GPa (Figure 4f). The sample shows a homogeneous elemental distribution, probably due to the higher stability of the intermetallic phase, acting as barrier to diffusion between grains. Spinodal decomposition does not occur and the hexagonal intermetallic fills the space between grains of the main phase. The number of cavities in the scandium containing sample is noticeably less than in the scandium-free sample. PXRD shows only the main *B2* phase, as the *W*-phase diffraction lines are partially masked by Al₂O₃ from the assembly (Figure 2d).

Sintering at 9.5 GPa results in complete densification of the sample (Figure 4h). Two events occur at 1020 and 1330 K, probably related to a change of ordering in the *B2* phase and the dissolution of the intermetallic. The diffraction lines corresponding to *fcc*₁, *cP* and *fcc*₂ are not present. The recovered alloy treated at 9.5 GPa and 1500 K displays a strikingly different microstructure compared with both as-cast and low-pressure materials. Not only Cr homogeneously distributed in the matrix, the scandium phase has partially dissolved in the matrix as well (Figure 4j). The result is confirmed by the disappearance of the diffraction lines characteristic for the *W*-phase in the sample sintered at 9.5 GPa and 1500 K (Figure 2d and 2e). Only the diffraction line belonging to MgO from the assembly can be detected in the region of interest (Figure 2f). Sample sintered at 18.5 GPa similarly do not show any traces of *W*-phase according to *ex situ* PXRD.

Currently, not many HEAs were investigated under HP–HT conditions. Existing compressibility parameters and thermal expansion data are summarized in Table 2. Primary, *fcc*-CoCrFeMnNi was intensively investigated up to 54 GPa at room temperature [39,55,56]. Surprisingly, this single phase *fcc* alloy shows complex behaviour under compression. Two publications suggest *fcc* to *hcp* transition accurse above 14 GPa [39,56]. Nevertheless, later work confirms phase stability of *fcc*-CoCrFeMnNi below 50 GPa [55]. Such contradicting results can correspond to slight changes in alloys compositions between mentioned works as well as can be explained by an-hydrostatic compression due to use of molten sample in a form of small flake. *Fcc*-CoCrFeMnNi samples, which undergo *fcc* to *hcp* phase transformation, give nearly identical bulk moduli. pressure stable

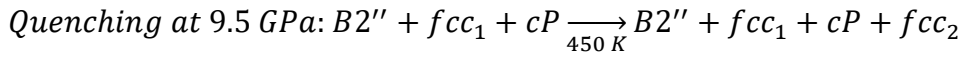
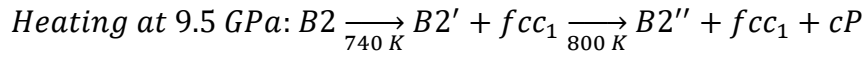
fcc-CoCrFeMnNi investigated in [55] shows no pressure-induced phase transition and has larger bulk modulus in comparison with samples investigated in [39] and [56], the sample has higher bulk modulus as well. As soon as actual composition of both alloys as well as their microstructures were not given in referenced papers we expect unreported differences between samples from independent studies. It seems that overall and local composition as well as samples history play important role in high-pressure stability of HEA's. Composition dependence of compressibility trends should be further investigated.

A presence of *fcc* to *hcp* transformation in *fcc*-CoCrFeMnNi suggests a possible phase instability in single-phase HEAs and stimulates further HP investigations of multicomponent alloys. In the present study, *fcc*-Al_{0.3}CoCrFeNi and *bcc*-Al₂CoCrFeNi were investigated up to 61 GPa under hydrostatic compression in DACs. Both alloys belong to the same family with only variation in Al content. Both alloys show phase stability and do not undergo any phase changes with compression. *Fcc*-Al_{0.3}CoCrFeNi has smaller atomic volume and larger bulk modulus, now has the record number among medium density HEAs (Table 2). *fcc*-CoCrFeMnNi also shows larger bulk modulus, $B_0 = 194$ GPa, in comparison with *bcc*-Hf_{0.25}Nb_{0.25}Zr_{0.25}Ti_{0.25} ($B_0 = 88$ GPa) [55]. Thermal expansion coefficients for *fcc*-Al_{0.3}CoCrFeNi and *bcc*-Al₂CoCrFeNi are comparable (Table 2).

The present work portrays a wide investigation of the parameters, which influence phase formation and stability in HEAs. The relatively mild experimental conditions used during SPS and in multi-anvil press are not enough to obtain a material of density comparable with the as-cast alloy. In fact, while densification by SPS is promoted by the current flow between particles, HEAs have been reported as having higher electrical resistivity values in comparison with conventional alloys [51]. The results obtained at 2.1 GPa (1253 K) and 9.5 GPa (1000 K) with respect to the one at 9.5 GPa and 1500 K highlight the prominent role of temperature over pressure in the densification of the *bcc*-Al₂CoCrFeNi powders. Plastic deformation and ultimate densification can only occur after appreciable bonding between particles has taken place. It is thus quite likely that densification

would be aided by the occurrence of an exothermal reaction, such as the formation of the *bcc*–Al₂CoCrFeNi from elemental powders.

The role of pressure and temperature is pivotal in every step of sample processing, because it deeply affects not only sintering process but also phase stability. The body of experiments points out to the exceptional stability of the *B2* phase from ambient pressure to 65 GPa, as the alloy does not undergo any pressure-driven phase transitions at room temperature. Conversely, heating the alloy at ambient pressure results in the exsolution of 40 % of the *B2* phase in two *fcc* phases (above 893 K). The behaviour of the alloy is very different when heating is performed under compression. The transformation occurring in the Al₂CoCrFeNi HEA can be summarized as follows:



The sample recovered after quenching consists of the *B2''* phase and 6 wt.% of other phases. The secondary phase, though minor, could contribute to the hardness enhancement via sintering effect with grain boundary pinning.

Homogeneous precipitates in alloys affect the HP–HT stability of the primary HEA phase. The Sc–containing MgZn₂–type secondary phase has previously been reported for Al–Cu–based alloys as detrimental to mechanical properties, since it inhibits the formation of the Al₃Sc intermetallic [52–54]. To study its interaction with a complex matrix can thus prove useful for further tuning of functional properties. At ambient pressure, the intermetallic leads to a 10 % hardness increase and delays the *B2* to *fcc* transition by an extra 150 K. The stabilization effect could be related to the higher thermal stability of the secondary phase, acting as barrier to diffusion through grain boundaries. While either pressure or compound precipitation can singularly delay the transition from *B2* to *fcc*, together they display a synergistic effect. The specimen containing 3 at.% Sc and pressed under a load of 9.5 GPa shows no traces of *fcc* phase and can be recovered as a pure *B2* phase. It displays a microstructure comparable to the original as-cast HEA, with a 20 % hardness increase. The dissolution of the intermetallic phase in the matrix at 9.5 GPa and 1500 K represents

one of the unique aspects of this system. The Sc-containing MgZn_2 -type phase is exceptionally stable, and its formation cannot be prevented by the high-entropy effect in multicomponent alloys. Nevertheless, HP–HT treatment results in its dissolution in the HEA matrix with the formation of a single-phase Sc-doped alloy. An adequate high-pressure high-temperature treatment could thus be functional in dissolving the analogous AlCuSc W -phase in Al–Cu alloys, while retaining the benefits of scandium additions upon quenching.

4. Conclusions

In the current study, specimens consisting of the $fcc\text{--Al}_{0.3}\text{CoCrFeNi}$ and $B2$ -structured single-phase $\text{Al}_2\text{CoCrFeNi}$ HEA without or with a 3 at.% scandium addition were studied in extreme temperature and pressure conditions. The application of pressure and the precipitation of a scandium intermetallic along grain boundaries can single-handedly enhance the stability of the alloy, but together display a synergistic effect which prevents the exsolution of secondary phases.

$fcc\text{--Al}_{0.3}\text{CoCrFeNi}$ and $bcc\text{--Al}_2\text{CoCrFeNi}$ are stable under compression at room temperature below 60 GPa. Bulk modulus at room temperature for $fcc\text{--Al}_{0.3}\text{CoCrFeNi}$ is higher in comparison with $bcc\text{--Al}_2\text{CoCrFeNi}$. $Bcc\text{--Al}_2\text{CoCrFeNi}$ at ambient pressure undergo phase transition above 800 K which does not occur under pressure which suggests an increase of phase stability with compression. Sc addition to $bcc\text{--Al}_2\text{CoCrFeNi}$ results in the precipitation of hexagonal AlScM W -phase between grains of bcc -structured matrix. The Sc-containing MgZn_2 -type phase is exceptionally stable, and its formation cannot be prevented by the high-entropy effect in multicomponent alloys. Nevertheless, HP–HT treatment results in its dissolution in the HEA matrix with the formation of a single-phase Sc-doped alloy. An adequate high-pressure high-temperature treatment could thus be functional in dissolving the analogous AlCuSc W -phase in Al–Cu alloys, while retaining the benefits of scandium additions upon quenching.

The results reported here open new possibilities in the design and further improvement of the properties of multicomponent alloys. They could be used as the basis for designing new stable and

metastable multicomponent single-phase alloys with improved mechanical properties. In the light of the unique properties of this system, more systematic studies should be performed, to better understand pressure-dependent transformations in multicomponent alloys. Composition-temperature-pressure equations of state, as well as modelling of temperature-pressure dependent multicomponent phase diagrams, can support further progress in the field.

Acknowledgements

The Authors gratefully acknowledge the financial support provided by the Welsh Government and Higher Education Funding Council for Wales through the Sêr Cymru National Research Network in Advanced Engineering and Materials and by the European Space Agency (contract number 4000111643/NL/PA). The authors thank the Materials Advanced Characterisation Centre (MACH1) at Swansea University, the DIAMOND light source (Oxfordshire, UK), the PETRA III (DESY, Hamburg, Germany) and the European Synchrotron Radiation Facility (Grenoble, France) for providing measurement time and technical support.

References

1. J.-W. Yeh, Recent progress in HEAs, *Ann. Chim. Sci. Mat.* 31 (2006) 633–648. DOI: 10.3166/acsm.31.633-648
2. B. Cantor, I.T. Chang, P. Knight, A.J.B. Vincent, Microstructural development in equiatomic multicomponent alloys, *Mater. Sci. Eng. A* 375–377 (2004) 213–218. <https://doi.org/10.1016/j.msea.2003.10.257>
3. J.-W. Yeh, S.-K. Chen, J.-W. Gan, S.-J. Lin, T.-S. Chin, T.-T. Shun, C.-H. Tsau, S.-Y. Chang, Formation of simple crystal structures in Cu–Co–Ni–Cr–Al–Fe–Ti–V alloys with multiprincipal metallic elements, *Metall. Mater. Trans. A* 35A (2004) 2533–2536. DOI: 10.1007/s11661-006-0234-4
4. U. Dahlborg, J. Cornide, M. Calvo-Dahlborg, T.C. Hansen, A. Fitch, Z. Leong, S.

- Chambreland, R. Goodall, Structure of some CoCrFeNi and CoCrFeNiPd multicomponent alloys by diffraction techniques, *J. All. Comp.* 681 (2016) 330–341.
<https://doi.org/10.1016/j.jallcom.2016.04.248>
5. L.J. Santodonato, Y. Zhang, M. Feygenson, C. M. Parish, M. C. Gao, R. J.K. Weber, J.C. Neuefeind, Z. Tang, P.K. Liaw, Deviation from high-entropy configurations in the atomic distributions of a multi-principal-element alloy, *Nat. Comm.* 6 (2015) 5964.
[doi:10.1038/ncomms6964](https://doi.org/10.1038/ncomms6964)
6. D. Li, Ch. Li, T. Feng, Y. Zhang, G. Sha, J.J. Lewandowski, P.K. Liaw, Y. Zhang, High-entropy Al_{0.3}CoCrFeNi alloy fibers with high tensile strength and ductility at ambient and cryogenic temperatures, *Acta Mat.* 123 (2017) 285–294 DOI: 10.1016/j.actamat.2016.10.038
7. G. Laplanche, A. Kostka, O.M. Horst, G. Eggeler, E.P. George, Microstructure evolution and critical stress for twinning in the CrMnFeCoNi high-entropy alloy, *Acta Mat.* 118 (2016) 152–163. <https://doi.org/10.1016/j.actamat.2016.07.038>
8. M.A. Hemphill, T. Yuan, G.Y. Wang, J.W. Yeh, C.W. Tsai, A. Chuang, P.K. Liaw, Fatigue behaviour of Al_{0.5}CoCrCuFeNi HEA, *Acta Mat.* 60 (16) (2012) 5723–5734.
<https://doi.org/10.1016/j.actamat.2012.06.046>
9. D.B. Miracle, O.N. Senkov, A critical review of high entropy alloys and related concepts, *Acta Mat.* 122 (2017) 448–511. <https://doi.org/10.1016/j.actamat.2016.08.081>
10. M.-H. Chuang, M.-H. Tsai, W.-R. Wang, S.-J. Lin, J.-W. Yeh, Microstructure and wear behavior of Al_xCo_{1.5}CrFeNi_{1.5}Ti_y high-entropy alloys, *Acta Mat.* 59 (2011) 6308–6317.
<https://doi.org/10.1016/j.actamat.2011.06.041>
11. S. Singh, N. Wanderka, B.S. Murty, U. Glatzel, J. Banhart, Decomposition in multi-component AlCoCrCuFeNi high-entropy alloy, *Acta Mat.* 59 (2011) 182–190.
<https://doi.org/10.1016/j.actamat.2010.09.023>
12. M.-H. Chuang, M.-H. Tsai, C.-W. Tsai, N.-H. Yang, S.-Y. Chang, J.-W. Yeh, S.-K. Chen, S.-J. Lin, Intrinsic surface hardening and precipitation kinetics of Al_{0.3}CrFe_{1.5}MnNi_{0.5} multi-

- component alloy, J. Alloy. Compd. 551 (2013) 12–18.
<https://doi.org/10.1016/j.jallcom.2012.09.133>
13. W.-H. Liu, Z.P. Lu, J.Y. He, J.H. Luan, Z.J. Wang, B. Liu, Y. Liu, M.W. Chen, C.T. Liu, Ductile CoCrFeNiMo_x high entropy alloys strengthened by hard intermetallic phases, Acta Mat. 116 (2016) 332–342. <https://doi.org/10.1016/j.actamat.2016.06.063>
14. S. Niu, H. Kou, T. Guo, Y. Zhang, J. Wang, J. Li, Strengthening of nanoprecipitations in an annealed Al_{0.5}CoCrFeNi high entropy alloy, Mat. Sci. Eng. A. 671 (2016) 82–86. <https://doi.org/10.1016/j.msea.2016.06.040>
15. F. He, Z. Wang, S. Niu, Q. Wu, J. Li, J. Wang, C.T. Liu, Y. Dang, Strengthening the CoCrFeNiNb_{0.25} high entropy alloy by FCC precipitate, J. Alloy. Compd 667 (2016) 53–57. <https://doi.org/10.1016/j.jallcom.2016.01.153>
16. J.M. Zhu, H.M. Fu, H.F. Zhang, A.M. Wang, H. Li, Z.Q. Hu, Synthesis and properties of multiprincipal component AlCoCrFeNiSi_x alloys, Mat. Sci. Eng. A 527 (27–28) (2010) 7210–7214. <https://doi.org/10.1016/j.msea.2010.07.049>
17. B.S. Li, Y.P. Wang, M.X. Ren, C. Yang, H.Z. Fu, Effects of Mn, Ti and V on the microstructure and properties of AlCrFeCoNiCu high entropy alloy, Mat. Sci. Eng. A 498 (1–2) (2008) 482–486. <https://doi.org/10.1016/j.msea.2008.08.025>
18. U.S. Hsu, U.D. Hung, J.W. Yeh, S.K. Chen, Y.S. Huang, C.C. Yang, Alloying behaviour of iron, gold and silver in AlCoCrCuNi-based equimolar high-entropy alloys, Mat. Sci. Eng. A 460–461 (2007) 403–408. <https://doi.org/10.1016/j.msea.2007.01.122>
19. Y.-F. Kao, T.-J. Chen, S.-K. Chen, J.-W. Yeh, Microstructure and mechanical property of as-cast, -homogenized, and -deformed Al_xCoCrFeNi (0 < x < 2) high-entropy alloys, J. Alloy Compd. 488 (1) (2009) 57–64. doi:10.1016/j.mseb.2009.05.024
20. S.S. Ghazi, K.R. Ravi, Phase-evolution in high entropy alloys: role of synthesis route, Intermet. 73 (2016) 40–42. <https://doi.org/10.1016/j.intermet.2016.03.002>
21. M. Park, C.A. Schuh, Accelerated sintering in phase-separating nanostructured alloys,

Nature Comm. 6 (2015) 6858. doi:10.1038/ncomms7858

22. P.F. Yu, L.J. Zhang, H. Cheng, H. Zhang, M.Z. Ma, Y.C. Li, G. Li, P.K. Liaw, R.P. Liu, The high-entropy alloys with high hardness and soft magnetic property prepared by mechanical alloying and high-pressure sintering, *Intermetallics* 70 (2016) 82–87. <https://doi.org/10.1016/j.intermet.2015.11.005>

23. Z.J. Jiang, J.Y. He, H.Y. Wang, H.S. Zhang, Z.P. Lu, L.H. Dai, Shock compression response of high entropy alloys, *Mat. Res. Lett.* 4 (4) (2016) 226–232. <http://dx.doi.org/10.1080/21663831.2016.1191554>

24. N.S. Weston, F. Derguti, A. Tudball, M. Jackson, Spark plasma sintering of commercial and development of titanium alloy powder, *J. Mat. Sci.* 50 (14) (2015) 4860–4878. <https://doi.org/10.1007/s10853-015-9029-6>

25. S. P. Thompson, J. E. Parker, J. Marchal, J. Potter, A. Birt, F. Yuan, R. D. Fearn, A. R. Lennie, S. R. Street and C. C. Tang, Fast XRPD on I11 at Diamond, *J. Synchr. Rad.* 18 (2011) 637–648. DOI: 10.1063/1.3167217.

26. A. P. Hammersley, S. O. Svensson, M. Hanfland, A. N. Fitch and D. Häusermann, Two-dimensional detector software: from real detector to idealised image or two-theta scan, *High Press. Res.* 14 (1996) 235–248. <http://dx.doi.org/10.1080/08957959608201408>

27. J. Perl, J. Shin, J. Schumann, B. Faddegon and H. Paganetti, TOPAS: an innovative proton Monte Carlo platform for research and clinical applications, *Med. Phys.* 39 (11) (2012) 6818–6837. doi: 10.1118/1.4758060

28. G. A. Sweet, M. Brochu, R. L. Hexemer Jr., I. W. Donaldson and D. P. Bishop, Consolidation of Al-based metal matrix composites via SPS, *Mat. Sci. Eng. A* 648 (2015) 123–133. DOI: 10.1016/j.msea.2015.09.027

29. F. R. Boyd and J. L. England, Apparatus for phase-equilibrium measurements at pressures up to 50 kilobars and temperatures up to 1750°C, *J. Geophys. Res.* 65 (1960) 741–748. DOI: 10.1029/JZ065i002p00741

30. J. Guignard and W. A. Crichton, The large volume press facility at ID06 beamline of the European synchrotron radiation facility as a High Pressure-High Temperature deformation apparatus, *Rev. Sci. Instrum.* 86 (8) (2015) 085112. doi: 10.1063/1.4928151
31. Y. Le Godec, D. Martinez-Garcia, M. Mezouar, G. Syfosse, J. P. Itié and J. M. Besson, Thermoelastic behaviour of hexagonal graphite-like BN, *High Press. Res.* 17 (1) (2000) 35–46. <http://dx.doi.org/10.1080/08957950008200304>
32. R. S. Pease, An X-ray study of boron nitride, *Acta Cryst.* 5 (1952) 356–361.
33. L. S. Dubrovinsky, S. K. Saxena, Thermal expansion of periclase (MgO) and tungsten (W) to melting temperatures, *Phys. Chem. Minerals* 24 (1997) 547–550. <https://doi.org/10.1007/s002690050070>
34. A. Dewaele, G. Fiquet, D. Andrault and D. Hausermann, P–V–T equation of state of periclase from synchrotron radiation measurements, *J. Geophys. Res.* 105 (2000) 2869–2877. DOI: 10.1029/1999JB900364
35. J.-P. Poirier, *Introduction to the Physics of the Earths Interior*, second ed., Cambridge University Press (Virtual Publishing), 2003.
36. H.-L. Wang, T.-X. Gao, J.-Z. Niu, P.-J. Shi, J. Xu, Y. Wang, Microstructure, thermal properties, and corrosion behaviour of FeSiBAlNi alloy fabricated by mechanical alloying and spark plasma sintering, *Int. J. Min. Metal. Mat.* 23 (1) (2016) 77–82. <https://doi.org/10.1007/s12613-016-1213-4>
37. S. Mohanty, N.P. Gurao, K. Biswas, Sinter ageing of equiatomic $\text{Al}_{20}\text{Co}_{20}\text{Cu}_{20}\text{Zn}_{20}\text{Ni}_{20}$ high entropy alloy via mechanical alloying, *Mat. Sci. Eng. A* 617 (2014) 211–218. <https://doi.org/10.1016/j.msea.2014.08.046>
38. A. Zhang, J. Han, J. Meng, B. Su, P. Li, Rapid preparation of AlCoCrFeNi HEA by spark plasma sintering from elemental powder mixture, *Mat. Lett.* 181 (2016) 82–85. doi:10.1016/j.matlet.2016.06.014

39. C.L. Tracy, S. Park, D.R. Rittman, S.J. Zinkle, H. Bei, M. Lang, R.C. Ewing, W.L. Mao, High pressure synthesis of a hexagonal close-packed phase of the high-entropy alloy CrMnFeCoNi, *Nature Commun.* 8 (2016) 15634. doi:10.1038/ncomms15634
40. M.S. Lucas, L. Mauger, J.A. Munoz, Y.M. Xiao, A.O. Sheets, S.L. Semiatin, J. Horwath, Z. Turgut, Magnetic and vibrational properties of HEA, *J. Appl. Phys.* 109 (2011). doi:10.1063/1.3538936
41. H.-P. Chou, Y.-S. Chang, S.K. Chen, J.W. Yeh, Microstructure, thermophysical and electrical properties in $\text{Al}_x\text{CoCrFeNi}$ HEA, *Mater. Sci. Eng. B* 163 (2009) 184–189. DOI: 10.1016/j.mseb.2009.05.024
42. C. Li, M. Zhao, J.C. Li, Q. Jiang, B2 structure of high-entropy alloys with addition of Al, *J. Appl. Phys.* 104 (2008) 113504. <http://dx.doi.org/10.1063/1.3032900>
43. W.-R. Wang, W.-L. Wang, S.-C. Wang, Y.-C. Tsai, C.-H. Lai, J.-W. Yeh, Effects of Al addition on the microstructure and mechanical property of $\text{Al}_x\text{CoCrFeNi}$ high-entropy alloys, *Intermetallics* 26 (2012) 44–51. <https://doi.org/10.1016/j.intermet.2012.03.005>
44. C. Li, J.C. Li, M. Zhao, Q. Jiang, Effect of aluminum contents on microstructure and properties of $\text{Al}_x\text{CoCrFeNi}$ alloys, *J. All. Compd.* 504 (2010) S515–S518. <https://doi.org/10.1016/j.jallcom.2010.03.111>
45. J. Lužnik, P. Koželj, S. Vrtnik, A. Jelen, Z. Jagličić, A. Meden, M. Feuerbacher, J. Dolinšek, Complex magnetism of HoDyYGdTb HEA, *Phys.Rev.B* 92 (2015) 224201. <https://doi.org/10.1103/PhysRevB.92.224201>
46. J. Groza, K. R. Anderson, M. Fendorf C. J. Echer, Surface oxide debonding in field assisted powder sintering, *Mat. Sci. Eng. A* 270 (2) (1999) 278–282. [https://doi.org/10.1016/S0921-5093\(99\)00197-5](https://doi.org/10.1016/S0921-5093(99)00197-5)
47. N. S. Weston, F. Derguti, A. Tudball, M. Jackson, Spark plasma sintering of commercial and development titanium alloy powders, *J. Mat. Sci.* 50 (14) (2015) 4860–4878. <https://doi.org/10.1007/s10853-015-9029-6>

48. M.C. Gao, J.-W. Yeh, P.K. Liaw, Y. Zhang, High-entropy alloys: fundamentals and applications. Springer, (2016).
49. Y.-F. Kao, S.-K. Chen, T.-J. Chen, P.-C. Chu, J.-W. Yeh, S.-J. Lin, Electrical, magnetic and Hall properties of $\text{Al}_x\text{CoCrFeNi}$ HEA, *J. All. Compd.* 509 (5) (2011) 1607–1614. <https://doi.org/10.1016/j.jallcom.2010.10.210>
50. D. Liu, H. Wen, D. Zhang, C. Wang, Y. Lin, Y. Xiong, T. Topping, J.M. Schoenung, E.J. Lavernia, Stress-enhanced grain growth in a nanostructures Al alloy during SPS, *Phil. Mag. Lett.* 94 (11) (2014) 741–748. <http://dx.doi.org/10.1080/09500839.2014.975295>
51. Y. Zhang, T.T. Zuo, Z. Tang, M.C. Gao, K.A. Dahmen, P.K. Liaw, Z.P. Lu, Microstructures and properties of HEAs, *Prog. Mat. Sci.* 61 (2014) 1–93. <https://doi.org/10.1016/j.pmatsci.2013.10.001>
52. S. Riva, K.V. Yussenko, N.P. Lavery, D.J. Jarvis, S.G.R. Brown, The scandium effect in multicomponent alloys, *Int. Mat. Rev.* 61(3) (2016) 203–228. <http://dx.doi.org/10.1080/09506608.2015.1137692>
53. S. Riva, C.M. Fung, J.R. Searle, R.N. Clark, N.P. Lavery, S.G.R. Brown, K.V. Yussenko, Formation and disruption of W -phase in HEAs, *Metals* 6 (5) (2016) 106. doi:10.3390/met6050106
54. B.A. Chen, G. Liu, R.H. Wang, J.Y. Zhang, L. Jiang, J.J. Song, J. Sun, Effect of interfacial solute segregation on ductile fracture of Al–Cu–Sc alloys, *Acta Mater.* 61 (2013) 1676–1690. <https://doi.org/10.1016/j.actamat.2012.11.043>
55. A. S. Ahmad, Y. Su, S. Y. Liu, K. Stahl, Y. D. Wu, X. D. Hui, U. Ruett, ^[11]_{SEP}O. Gutowski, K. Glazyrin, H. P. Liermann, H. Franz, H. Wang, X. D. Wang, Q. P. Cao, D. X. Zhang, and J. Z. Jiang, Structural stability of high entropy alloys under pressure and temperature, *J. Appl. Phys.* 121 (2017) 235901. doi:10.1063/1.4984796.

56. F. Zhang, Y. Wu, H. Lou, Zh. Zeng, V.B. Prakapenka, E. Greenberg, Y. Ren, J. Yan, J.S. Okasinski, X. Liu, Y. Liu, Q. Zeng, and Zh. Lu, Polymorphism in a high-entropy alloy, *Nature Commun.* 8 (2016) 15687. doi:10.1038/ncomms15687

Figure 1. Room temperature compressibility for *bcc*-Al₂CoCrFeNi and *fcc*-Al_{0.3}CoCrFeNi. Insert shows ambient pressure thermal expansion for *bcc*-Al₂CoCrFeNi.

Figure 2. Resume of PXRD profiles obtained for *bcc*-Al₂CoCrFeNi and *bcc*-Al₂CoCrFeNi + 3 at.% Sc. PXRD profiles of *bcc*-Al₂CoCrFeNi (a) *in situ* ambient pressure heating (data collected at room temperature, 850°C and 1000°C, correspondently), (c) measured after ambient pressure annealing and SPS, (e) before, during and after *in situ* 9.5 GPa heating. PXRD profiles of *bcc*-Al₂CoCrFeNi + 3 at.% Sc (b) during *in situ* ambient pressure heating, (d) measured after ambient pressure sintering at 2.1 GPa and 18.5 GPa, (f) before, during and after *in situ* 9.5 GPa heating. PXRD profiles are plotted as function of $1/d$ to compare data obtained from DIAMOND (I11, $\lambda = 0.494984$ Å), ESRF (ID06, $\lambda = 0.22542$ Å) and in house instrument (CuK _{α 1}, $\lambda = 1.54059$ Å).

Figure 3. Temperature dependent (from room temperature to 1500 K at 9.5 GPa) PXRD patterns for (a) *bcc*-Al₂CoCrFeNi and (b) *bcc*-Al₂CoCrFeNi + 3 at.% Sc. The appearance of the secondary *fcc* phase at *ca.* 740 K is clearly visible in (a). (c) *bcc*-Al₂CoCrFeNi sample recovered after 9.5 GPa compression, quenched from 1500 K. The calculated profile (blue line) is shifted down from experimental data (black line) for clarity, difference is shown below. The profile can be fitted with a *B2* and an *fcc* phase. (d) *bcc*-Al₂CoCrFeNi + 3 at.% Sc sample recovered after 9.5 GPa compression, quenched from 1000 K. The MgZn₂-type *W*-phase is highlighted. (e) *bcc*-Al₂CoCrFeNi + 3 at.% Sc sample recovered after 9.5 GPa compression, quenched from 1500 K. (PXRD patterns collected *in situ* in the large-volume press (ESRF ID06-LVP, $\lambda = 0.22542$ Å, lines marked with star in the figure correspond to the assembly); # correspond to (100) line of *B2* phase).

Figure 4. SEM and EDX maps of: *bcc*-Al₂CoCrFeNi as-cast without Sc (a) and with a 3 at.% Sc addition (b); after annealing without Sc (c) and with 3 at.% Sc (d); after spark plasma sintering without Sc (e) and with 3 at.% Sc (f); after HP-HT sintering at 2.1 GPa without Sc (g) and with 3 at.% Sc (h); and after quenching from 1500 K, 9.5 GPa without Sc (i) and 3 at. % Sc (j).

Figure 5. Vicker's hardness values for the *bcc*-Al₂CoCrFeNi (blue) and *bcc*-Al₂CoCrFeNi + 3 at.% Sc (green) alloys.